UNIVERSITY OF CALIFORNIA,
IRVINE

Computational Methods as a Supplement to Atomic Force Microscopy

DISSERTATION

submitted in partial satisfaction of the requirements
for the degree of

MASTER OF SCIENCE

in Physics

by

Robert Noboru Sanderson

Dissertation Committee:

Associate Professor Regina Ragan, Chair
Professor Ruqian Wu
Professor Michael Dennin

2017

DEDICATION

For Jamie and Maxwell

TABLE OF CONTENTS

FIGURES AND TABLES

FIGURES

Page

TABLES

ACKNOWLEDGEMENTS

I would first like to thank my thesis advisor, Dr. Regina Ragan of the Department of Chemical Engineering and Materials Science. Her guidance in research and writing has been invaluable to me, and it has been a privilege to work with her.

I would also like to thank the members of the Ragan Laboratory, past and present, who provided important insight and helpful discussions about many of the topics in this thesis.

ABSTRACT OF THE DISSERTATION

Computational Methods as a Supplement to Atomic Force Microscopy

By

Robert Noboru Sanderson

Master of Physics and Astronomy

University of California, Irvine, 2016

Professor Regina Ragan, Chair

The atomic force microscope (AFM) is a widespread tool for the study of surfaces, as it allows for the unobtrusive measurement of nanoscale topography. AFM is also versatile, with variants that allow for the measurement of other quantities such as the local surface potential and Young's modulus. A hurdle to the use of AFM systems is that interpretation of force probe data is nontrivial due to non-idealities of experimental systems including noise and artifacts. This thesis covers two computational techniques to overcome the limitations of AFM systems. First, finite element method simulations are used in conjunction with KPFM studies of vapor-liquid-solid grown silicon nanowires. The nanowires are studied with a variable electric bias applied across them, analogous to a field-effect transistor in operation. Then, batch analysis is applied to extract mechanical information from large amounts of AFM force spectroscopy data from tethered lipid bilayer membrane systems, which are important model systems for studying the mechanics of cell membranes.

CHAPTER 1: INTRODUCTION

The work presented in this thesis uses computational methods to clarify experimental data obtained in two variants of atomic force microscopy (AFM). AFM has become a ubiquitous experimental technique in surface science due to its capability to produce high resolution topographical maps of nanoscale surfaces while causing little surface damage[1]. AFM systems are also versatile, and can be adapted to perform a variety of specialized experiments, including Kelvin probe force microscopy and AFM force spectroscopy. AFM techniques such as these have been used to characterize the surfaces of many systems including cells[2–6], lipid membranes[7,8], heterogeneous catalysts[9–11], nanoelectronics[12,13], and nanoscale systems[14–17].

The Kelvin probe force microscope allows for the measurement of local variations in work function. The non-contact nature of AFM makes this method uniquely suited to measuring work function without damage or significant interaction between probe and sample. These advantages have drawn strong interest in Kelvin probe force microscopy applied to insulators[18,19], photovoltaics[20,21], organic molecules[22,23], and devices[24–26].

AFM force spectroscopy allows a user to gain information on the local mechanical properties of surfaces, such as their elastic modulus[27,28]. AFM force spectroscopy uses extremely sharp probe tips which allow for very localized probing of a sample. Force spectroscopy is used in a wide array of fields, including polymer chemistry[29], nanomedical devices[30], electrochemistry[31], and cell membrane mechanics[7,32].

Both of these techniques have experimental limitations that hinder full understanding of experimental data. Interpretation of Kelvin probe data is made difficult because of background

non-local signals, a phenomenon known as the averaging effect[33,34] as well as capacitive contributions from the cantilever and tip cone[35]. These probe-based contributions to the measured work function are difficult to distinguish from real variations in the local surface potential. In FS, error is introduced by instrument limitations, vibrational noise, shortcomings of theoretical models, as well as local variations of a sample[36,37]. Computational studies performed in conjunction with these experiments reduce experimental uncertainty by quantifying known experimental aberrations and extracting meaningful physical information from experimental data[34,38,39]. The goal of this thesis is to present two applications of computational methods to improve the quantitative understanding of force microscopy data. Kelvin probe measurements are supplemented with finite element method simulations to identify the origin of detected local potential features and force spectroscopy results are analyzed using batch analysis and compared to theoretical models to obtain stiffness measurements.

In Chapter 2, this thesis will give a theoretical background to the AFM methods used in the presented work. The operating principles of AFM and Kelvin probe force microscopy are overviewed, and then the principles of AFM force spectroscopy are presented.

In Chapter 3, a Kelvin probe experiment is interpreted with the aid of computational methods. Finite element method simulations are utilized to interpret measurements of the local electronic potential of nanowire systems. Nanowires are an important topic in device research, with applications in piezoelectronics[40], lasers[41,42], supercapacitors[43], catalysis[44,45], and nanoelectronics[46–48]. In this chapter, n-doped Si nanowires are studied using Kelvin probe force microscopy, and the surface potential is measured for each of several applied bias voltages across the nanowires. The results of finite element method modeling of the nanowire/probe system are then used to clarify the contributions to the measured surface potential.

In Chapter 4, tethered lipid bilayer membrane systems are studied using force spectroscopy, and batch analysis is used to interpret the measured spectra. The mechanical behavior of lipid membranes is an important topic in cell morphology[49], neurodegenerative disorders[50], viruses[51], and medicine[30,52,53]. Solid-supported lipid bilayer membranes are popular model systems for biological applications, as their two dimensional structure facilitates manipulation and measurement[54–57]. The bilayer membranes are synthesized with varying concentrations of attached functional groups modifying the membranes. These functional groups are large structures chemically bonded to the LBMs, so are expected to change the mechanical stability of the membranes as their concentration changes. In this work, the concentration of functional groups is varied, and the mechanical stiffness of the LBMs is investigated using FS. Batch analysis is used to filter and analyze large sets of FS data to obtain measurements of the Young's modulus of the LBM systems.

The thesis then concludes with a discussion of the techniques presented here and their merits as supplementary tools for the AFM experimentalist.

CHAPTER 2: FORCE PROBE METHODS

2.1: Atomic Force Microscopy and Kelvin Probe Force Microscopy

In non-contact AFM, a sharp probe tip is raster scanned across the surface of a sample. The tip is attached to a vibrating cantilever beam with a known resonance frequency f_0. Interaction forces act between the probe and sample when they are very near each other, and a force gradient acting on the tip due to tip-sample interactions will cause a change in the probe cantilever's resonance frequency approximated by[58]:

$$\Delta f_0 = -\frac{f_0}{2k}\frac{\partial F_{ts}}{\partial z}. \qquad \text{Equation 1}$$

In this expression, z is the tip position normal to the sample's surface, and the cantilever/tip system is considered a harmonic oscillator with spring constant k. It is seen that a force gradient translates to a change in the resonant frequency of the cantilever. Figure 1 shows the standard simplified model of the tip-sample interaction potential; the Lennard Jones interaction potential, given by

$$U_{LJ}\ \alpha\ (\frac{\sigma_0}{r})^{12} - (\frac{\sigma_0}{r})^{6}. \qquad \text{Equation 2}$$

If one chooses a tip-sample separation corresponding to the highlighted region in the figure, it is found that the vibrational frequency of the cantilever/tip system increases as the tip-sample separation increases and *vice versa*. Two modes of operation are frequently used which take advantage of this behavior: Amplitude modulation mode (AM-AFM) and frequency modulation mode (FM-AFM) of which only AM-AFM is considered in this thesis.

In AM-AFM, the cantilever is excited near resonance with constant drive amplitude. As the tip is scanned across a sample, changes in tip-sample separation cause changes in the force gradient, which causes a change in resonant frequency. This change in cantilever resonance is detected as a decrease in cantilever oscillation amplitude. A feedback loop is used to adjust the tip's z-position to bring the oscillation amplitude back to its target value, thereby measuring the local topography change. Recording the changes in the tip-sample separation yields a topographical map of the sample.

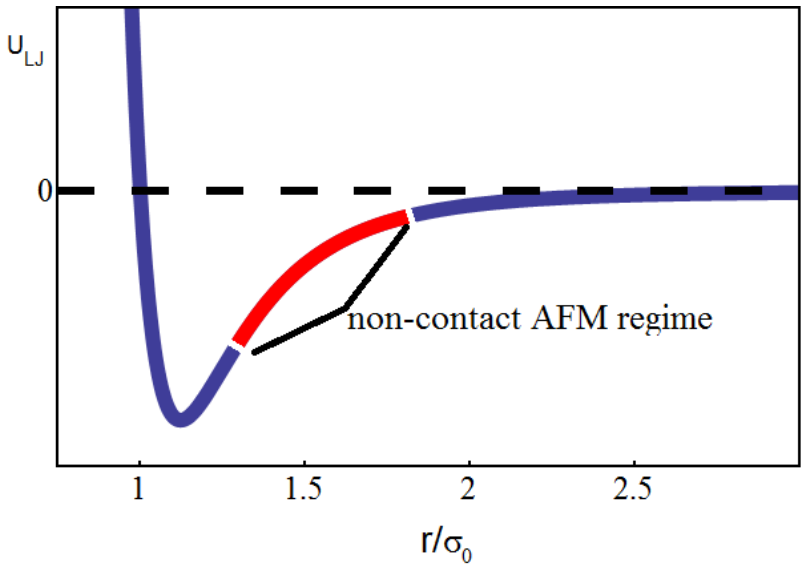

Figure 1 — Lennard-Jones Potential: The Lennard-Jones interaction potential provides a qualitative description of the tip-sample interaction in AFM. Highlighted in red is the region of interest during non-contact AFM experiments. $\boldsymbol{\sigma_0}$ is a characteristic length, and the potential U_{LJ} is in arbitrary units.

KPFM is performed using the same basic apparatus as an AFM, except since this technique is sensitive to electrostatic interactions rather than the Lennard Jones interaction of Equation 2, a conductive probe tip must be used to control the electrostatic potential of the probe.. In two-pass KPFM, AFM first determines the surface topography of a scan line, and then a second pass with a new feedback loop to minimize the electrostatic force by varying the tip-

sample bias determines the local contact potential difference (CPD) between the probe and the sample. This allows for a detailed map of the CPD, which is essentially the local work function superposed with any other electronic potential variations.

Although KPFM is useful in mapping electronic structure, it is prone to experimental artifacts[22,27,28]. The electrostatic forces to which KPFM is sensitive are longer range than the Van der Waals interactions which dominate AFM studies, decaying as R^{-2} rather than R^{-7}. This long range behavior convolutes KPFM maps, making observed features a weighted average of surface potential features. This phenomenon makes careful interpretation of CPD measurements in KPFM essential in extracting useful information from the data. To accomplish this, computational work work as a supplement to atomic force studies has been demonstrated. Analytic computations from first-principles of simplified surface/probe systems have been used to understand the fundamental behavior of KPFM work[33,60]. Numerical simulations have also been used to approximate the probe/sample systems[34,38,61,62]. The inhomogeneous systems that are of interest to researchers studying devices are too complex to model analytically[38,62–64], so numerical approximations are more appropriate.

Finite element method (FEM) simulations are well suited to model complex geometries. . In FEM simulations, system geometries are divided into a finite number of elements, and continuous variables are discretized, and made constant within each of these elements. In this manner, the potential distributions in electrostatic systems with complex geometries that often arise in Kelvin probe experiments involving devices can be approximated. KPFM measurements of various nanoscale potential distributions[34], surface topographies[38], and other phenomena such as grain boundaries[61,65] have been successfully modeled by using FEM simulations. By coupling FEM simulations with experimental data, it is possible to gain a better understanding of the

surface topography and electronic structure of a surface when performing AFM/KPFM experiments.

2.2: Force Spectroscopy

FS is a family of experimental techniques that uses a mechanical force to probe the properties of a material. The work in this thesis focuses on FS on lipid bilayer membrane (LBM) samples performed using an atomic force microscope and all subsequent references to FS will refer to AFM-based FS of LBM systems. Here, an AFM probe tip is pressed down through a LBM and then retracted. The force data, the piezoelectric voltage data, and the tip deflection data are stored for analysis.

Correct interpretation of FS data requires an understanding of the dynamics of the AFM cantilever. Figure 2 shows schematically how the cantilever behaves during a FS experiment using a LBM on a hard substrate. In (a), the cantilever position z is adjusted to indent the tip into the sample. When contact is made, the cantilever beam deflects a distance d. The difference $|z|$-$|d|$ is the indentation distance δ, the position of the tip relative to the sample surface. The distance δ is the most widely used measurement value in AFM FS literature[66]. A closer view of the tip-sample interaction is shown in (b). The tip is brought into contact with the LBM, and pushed through it. The tip force as a function of δ for a sample FS experiment is shown in Figure 2(c). For large δ values, there is minimal force, since the tip does not interact with the surface. The vertical data points at $\delta = 0$ (Point A) indicate contact with the hard substrate. The jump between Point B and Point A is a breakthrough event, where the probe tip tears through the LBM. Point C is the initial contact between tip and sample. These force/indentation spectra are useful measurements in FS, because they allow for the measurement of certain material

properties of a surface. For instance, the rate at which the force increases with increased indentation (Point C) is related to the Young's modulus of the LBM. The exact relation needed to compute the Young's modulus is not simple, as it depends on tip geometry, tip-sample interactions, and LBM composition.

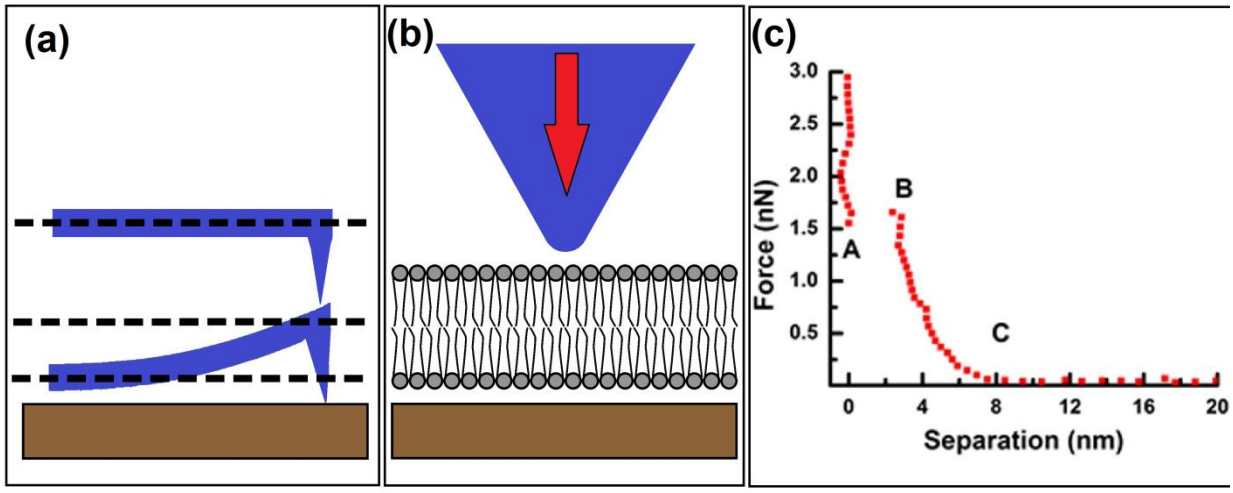

Figure 2 — Force Spectroscopy on Lipid Bilayers: (a) Schematic of cantilever behavior during FS. Tip-sample separation is calculated by taking the difference between the cantilever's displacement and its deflection. (b) Schematic representation of a tip being indented into a LBM during a FS experiment. (c) Force as a function of calculated tip-sample separation.

Models for tip force as a function of indentation have been the subject of much research in research years because of the rise of AFM FS as a materials characterization technique[2–8]. The Sneddon model isone such model that models a cone indenting into a semi-infinite elastic material[67]:

$$F_{Sneddon} = \frac{2}{\pi}\tan\theta\,\frac{E}{1-\nu^2}\delta^2.$$

Equation 3

This expression relates the tip-sample force F to the indentation distance δ of the tip into the sample, with θ being the conical tip's opening angle, ν the Poisson ratio of the sample, and E the Young's modulus of the sample. The Sneddon model is a good approximation for the behavior of an elastic material, but it does not take into account the stiffness variation between the substrate and tLBM, causing the model to overestimate the membrane's Young's modulus. A modified model that accounts for the substrate stiffness, known as the bottom effect cone correction (BECC) model, is[36]:

$$F_{BECC} = \frac{8}{3\pi} E \tan\theta\, \delta^2 (1 + 1.7795\, \frac{\tan\theta}{\pi^2} \frac{\delta}{h} + 16(1.7795)^2 tan^2\theta\, \frac{\delta^2}{h^2}). \quad \text{Equation 4}$$

In this adapted model, the finite thickness of the LBM is taken into account by considering an elastic membrane of thickness h on top of a semi-infinite rigid substrate.

Using these two models, the elastic modulus was computed for tLBMs using FS experimental data. Least-square fits of the force versus indentation data to the Sneddon and BECC models determine the elastic modulus of sample LBMs. A flow chart showing the basic logic behind the analysis of a single force-distance curve is shown in Figure 3. First, the force-distance data in the form of tab-separated text is imported as a list of ordered pairs and filtered to remove aberrational curves, such as those containing vibrational artifacts or multiple breakthrough events indicating overlap of LBMs. Three points of physical significance are then algorithmically determined: The hardwall contact point, the breakthrough point, and the contact point. The hardwall contact point corresponds to the point where the force versus indentation slope becomes infinite when the tip comes in contact with the hard substrate. The breakthrough point is the last point during the tip's approach before the tip overcomes the LBM's intra-membrane forces and breaks through, as signified by a sudden change of slope in the force-

distance curve. The contact point is the point when the probe tip first comes in contact with the membrane surface. The locations of these points are determined and stored to be used in the modulus computations. The difference between the breakthrough point position and the hardwall contact point position is referred to as the breakthrough distance. An estimate for the total membrane thickness, computed as the difference between the contact point position and the hardwall contact point position, is referred to in this work as the onset compression distance. Finally, the data near the contact point are used in a native Mathematica fitting function to solve for the Young's modulus using either the Sneddon model (Equation 3) or the BECC model (Equation 4), with appropriate parameter values substituted ($\theta = 35°$, $\nu = 0.5$, and h is given by the onset compression value.

Once this computation is completed for all sets of data, we can proceed to data analysis. The code used in this work calculated the breakthrough distance, onset compression distance, and Young's modulus for the LBM systems, allowing for a detailed analysis of changes in their stiffness and membrane strength.

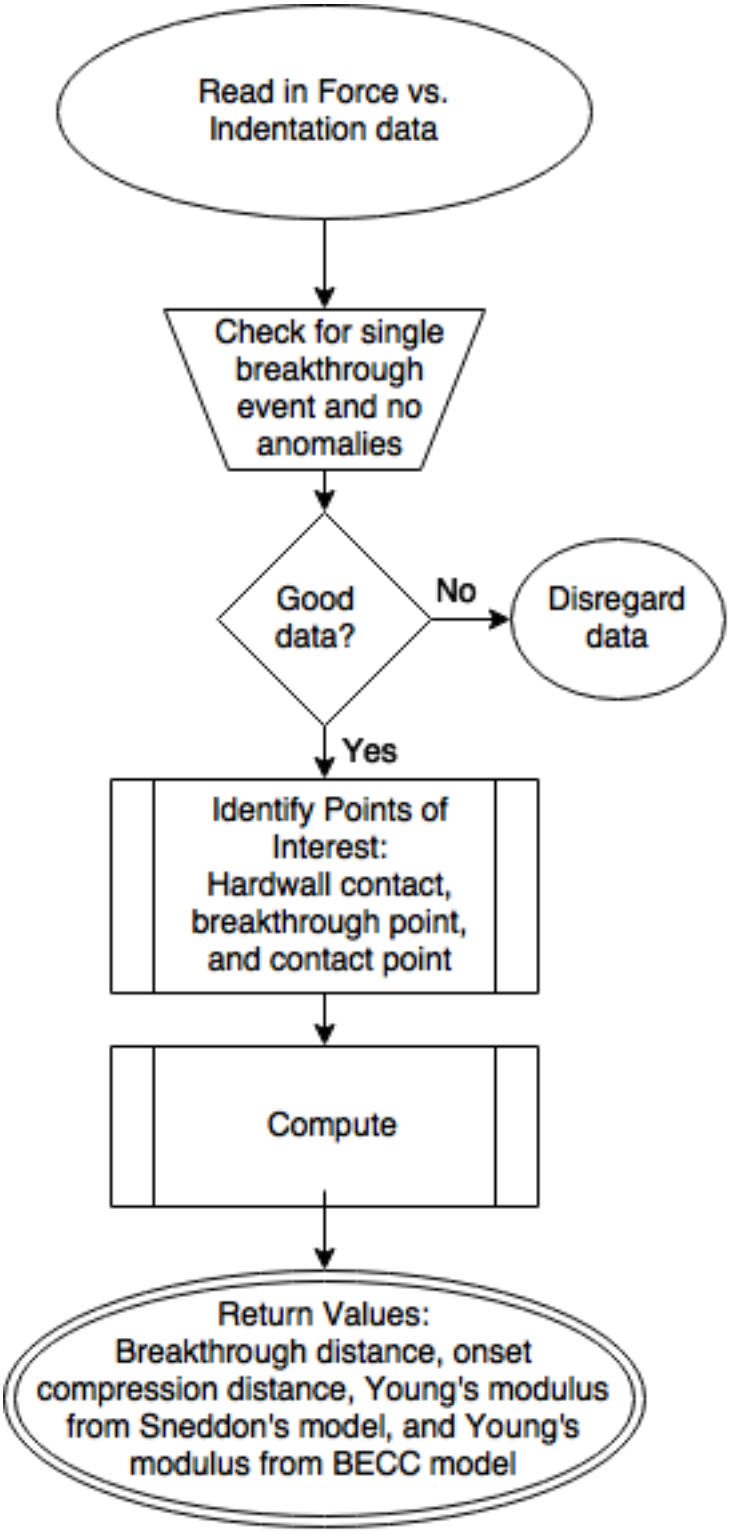

Figure 3 — Modulus Calculation Flow Chart:

CHAPTER 3: FEM-SUPPLEMENTED KPFM

Interpreting Kelvin Probe Force Microscopy of Current-Carrying Nanowires

Nanowires (NWs) are an important topic in device research, with many different applications [40–48]. Vapor-liquid-solid deposition is a versatile technique used to produce NWs, and still used to produce various sensors, batteries, and solar cells[68–70]. Nanowires grown using VLS deposition, shown schematically in Figure 4, were studied using AFM and KPFM. Si electrodes were created by etching a 100nm thick n-type Si layer on a SiO_2/Si substrate, and then were passivated with a layer of Si_3N_4. Au nanoparticles were then deposited at the electrode/trench interface to catalyze the growth of Si nanowires across the trench. Other work[71] details the growth process in more detail, though the nanowires used in this study are different in that they did not have a top metal gate on the nanowire, and they had an approximately 3nm thick SiO_2 oxide layer.

AFM topography and KPFM CPD data for two such nanowires are shown in Figure 5 and CPD line profiles across the nanowire labeled "NW2" for various applied potentials are shown in Figure 6. From Figure 5(c), the applied bias is seen by comparing the measured CPD on the two electrodes, however bright ridges appear at the electrode-trench interfaces. These are also seen in the zero-bias case (Figure 5(b)). These peaks can be seen in more detail in the line profiles of Figure 6. Correct interpretation of this data is important to understand the experimental system, but it is a nontrivial process.

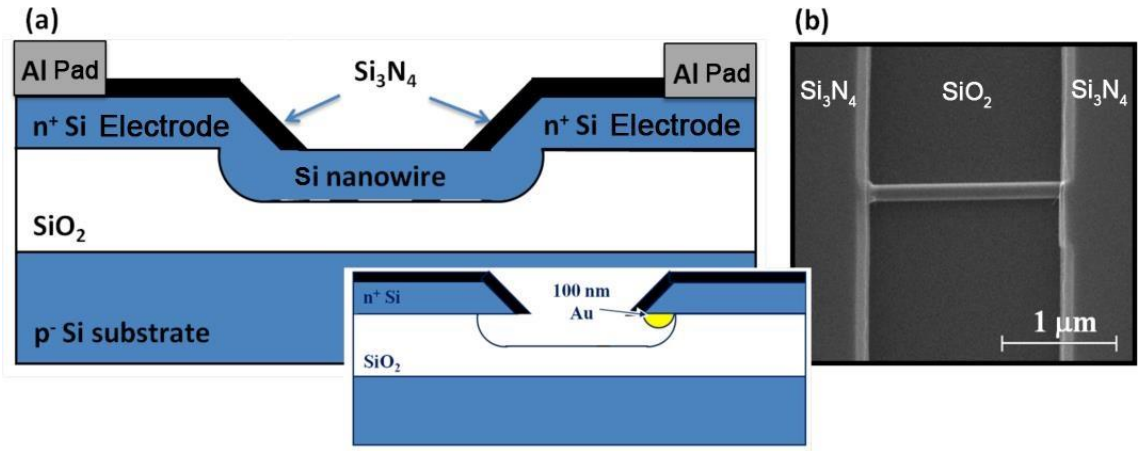

Figure 4 — Vapor-Liquid-Solid Nanowires: Schematic cross-section of a VLS nanowire and (inset) a schematic of an Au particle used to catalyze the growth of a nanowire. (b) SEM image of one of these nanowires.

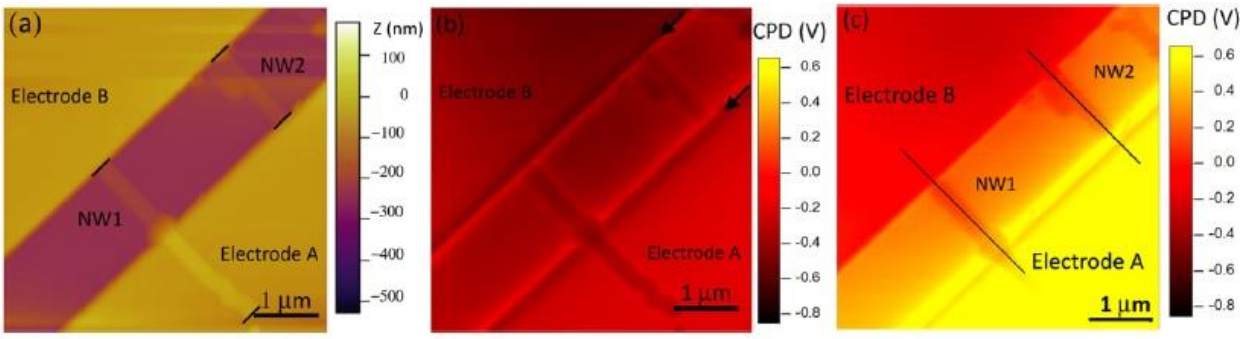

Figure 5 — VLS Nanowire Scanning Probe Measurements: (a) AFM topography map of two VLS nanowires NW1 and NW2, with black lines signifying the ends of each nanowire. (b) CPD map with VAB = 0V and (c) at VAB = 1V. Black lines in (c) show locations of CPD line profiles shown later.

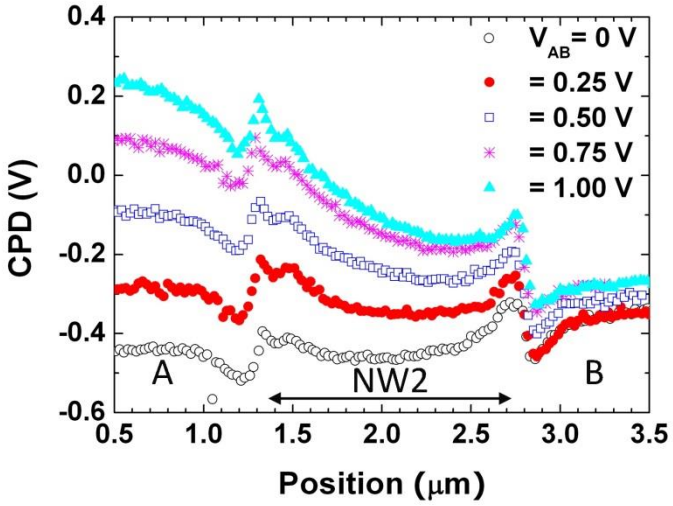

Figure 6 — VLS Nanowire CPD line profile: CPD values measured across a VLS nanowire spanning from electrodes labeled "A" and "B" with various applied biases.

KPFM CPD maps of these nanowires are challenging to interpret for a number of reasons. The topography of the sample can introduce experimental artifacts. If the probe tip does not track the sample surface perfectly, and the tip is closer or further from the surface than expected, experimental artifacts will arise due to changes in the signal-to-background ratio[38,64]. This is likely to happen in topographically inhomogeneous samples, especially when there are steeply varying features such as the electrode/trench interface. There are also a number of different materials on the surface, and KPFM is sensitive to the local work function in a sample. These contributions to the local electronic potential can potentially confound the results of KPFM. The presence of insulating materials also makes data interpretation difficult, as trapped charge changes the local electronic potential. This makes KPFM of insulators such as SiO_2 a challenge[19]. These features convolute measurements of the local electronic potential of a sample, making it important to bear in mind the various sources of measured CPD variations.

The contributions to the CPD measurements taken from these VLS nanowire systems were identified using FEM simulations. The COMSOL Multiphysics software package was used to model the electrostatic behavior of a model Si nanowire. Two contributions to the anomalous CPD signals were investigated: The tip-sample separation and trapped charge at the electrode/trench interface.

The experimental system was modeled near a single nanowire 100 nm in diameter spanning a SiO_2 trench 1.5 μm wide between two Si electrodes with an insulating Si_3N_4 coating, similar to the schematic shown in Figure 4(a). The tip used during surface characterization (Olympus AC160TS) was approximated as a conical frustum joined with a sphere of the same nominal radius of curvature as the experimental tip. Standard material properties were used in each domain, and potential boundary conditions were applied to simulate the applied bias between the electrodes and the current traveling along the nanowire.

The impact of incorrect surface tracking on CPD measurements in KPFM has been demonstrated[38]. If a probe tip tracks closer to a sample surface at certain locations than others, the detected CPD can be different due to a different signal-to-background ratio, so FEM simulations were used to investigate the effect of varying the tip-sample separation at the electrode/trench interface, where the topography changes most drastically. In these simulations, the CPD was calculated and line profiles were produced near the positive electrode/nanowire interface for effective tip-sample separations of 20nm, 30nm, and 40nm. The results of this simulation are shown in Figure 7. It is seen that there are only minor changes in the CPD as the tip-sample separation is doubled. Incorrect tracking of the surface is thus not likely to account for the large potential peaks seen in Figure 6.

To investigate whether interface states at the nanowire/trench interface were responsible for the potential peaks shown in the KPFM line profiles, simulations were performed with a positive line charge inserted along the SiO_2/Si_3N_4 interface, for both 0.5V applied across the electrodes and for 0V. The resulting simulated line profiles across the nanowire trench in the presence of this interface charging is shown in Figure 8(a), along with the corresponding voltage-normalized curve (b). Potential spikes at the nanowire/electrode interface similar to those seen in Figure 6 are seen in the non-normalized curve, and are removed by normalization.

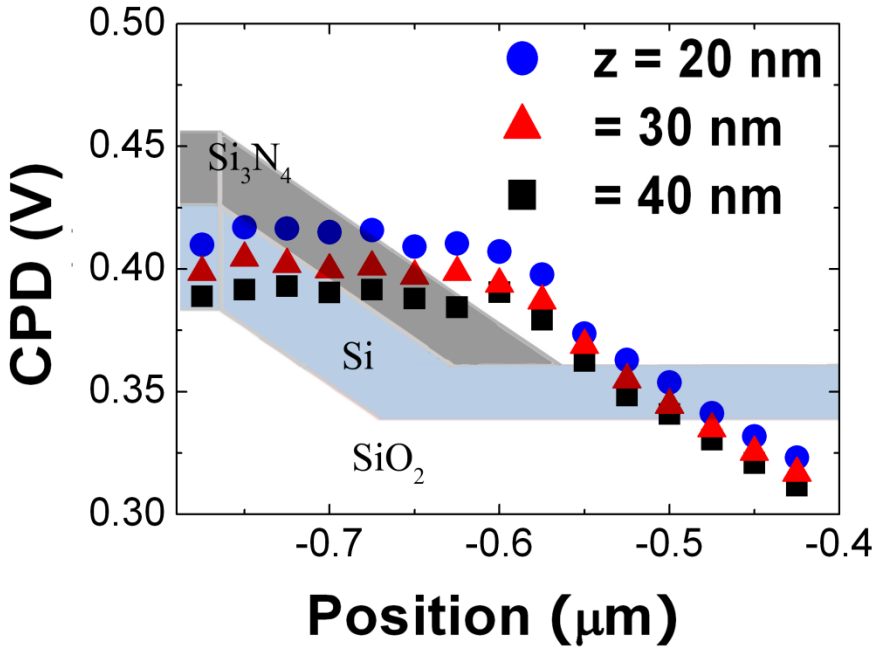

Figure 7 — FEM-calculated CPD partial line profiles: CPD line profiles near the nanowire/electrode interface, calculated using FEM simulations for differing tip-sample separations (z).

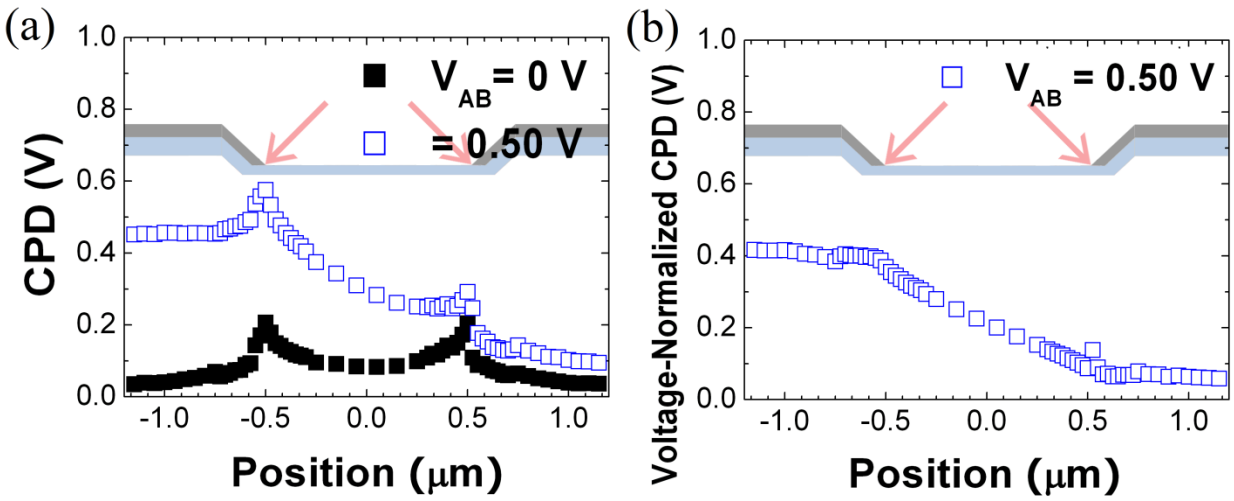

Figure 8 — Simulating interface charge states: (a) Simulated line profiles across a NW with positive interface charge inserted at the lowest point of the Si_3N_4 (indicated with red arrows in the schematic). (b) Voltage-normalized CPD line profile (obtained by taking the point-by-point difference between the two curves in (a)).

These simulations help to clarify the physical origin of the experimental features at the nanowire/electrode interface by using first-principles electrostatic calculations. The differentiation between experimental data and artifacts is an essential part of KPFM experimentation, and these simulations allow for a more quantitative understanding of otherwise ambiguous signals. By varying the tip-sample separation and computing CPD line profiles (Figure 7), it was demonstrated that the nanowire interface states were not likely caused by a scanning artifact from incorrect surface tracking. Furthermore, the simulations (Figure 8) also showed the possibility that trapped charge could cause the potential spikes seen in Figure 6.

The charge detected at the Si_3N_4/Si interface is not surprising, as the junction between these two materials has been long studied as a charge storage medium for application in memory storage devices[72]. The nanowire trench in the present study was etched using reactive ion

etching, and so it is likely that this process embedded charge in the Si_3N_4/Si interface during this etching process.

With the results of FEM simulations, it is now possible to perform more normalization techniques on the KPFM data to gain a deeper understanding of the electronic behavior of these systems. In Figure 9(d), it can be seen that NW I is not connected to the lower electrode. To investigate if there is a way to procedurally identify this nanowire as non-current-carrying, normalization techniques were applied. Figure 9(b) shows the voltage-normalized line profiles for NW I, and Figure 9(c) shows what the authors call the oxide-normalized line profiles. These are obtained by first taking CPD line profiles across the bare SiO_2 trench, shown in (e), and voltage normalizing them. These voltage-normalized oxide line profiles, pictured in (f), are then subtracted from the voltage-normalized line profiles along the nanowire. From (c), it is seen that the potential is uniformly zero, with the exception of the local work function change caused by a Au NP present near electrode B. This indicates that via normalization we have accounted for all of the contributions to the measured CPD. The disconnected nanowire therefore behaves similarly to the oxide background, and so the detected CPD in these NWs is primarily due to the capacitive response of the insulating SiO_2 substrate to the applied bias.

Oxide normalization of KPFM measurements was then carried out on current-carrying NWs, shown in Figure 10. Voltage-normalization is performed, and then oxide normalization, shown in (a) - (c). It is seen in (c) that the current-carrying NW II has a bias-dependent change in oxide-normalized CPD along the nanowire. The same behavior is observed in NWs III and IV, pictured in (d) and (e). The results from the oxide-normalized CPD line profiles therefore allow for the measurement of the change in electron density of current-carrying NWs as a function of applied potential.

This chapter demonstrated the use of computational methods in conjunction with normalization techniques to effectively and unobtrusively investigate NW systems. AFM and KPFM experimental data were interpreted to gain quantitative insight into the nanoelectronic behavior of these systems. First, FEM simulations were used to identify the physical origin of anomalous spikes in the measured CPD near NW-electrode interfaces as trapped charge introduced by the sample preparation process. Simulations were also used to justify the process of voltage normalization, which revealed nearly linear potential drops across the NWs, as expected for uniform NWs. Oxide normalization was then performed to provide a means of measuring the relative charge density on NWs. It has therefore been demonstrated that KPFM in conjunction with simulations is a powerful, facile, and contact-free method to probe surface electronic properties of nanodevices under operating conditions.

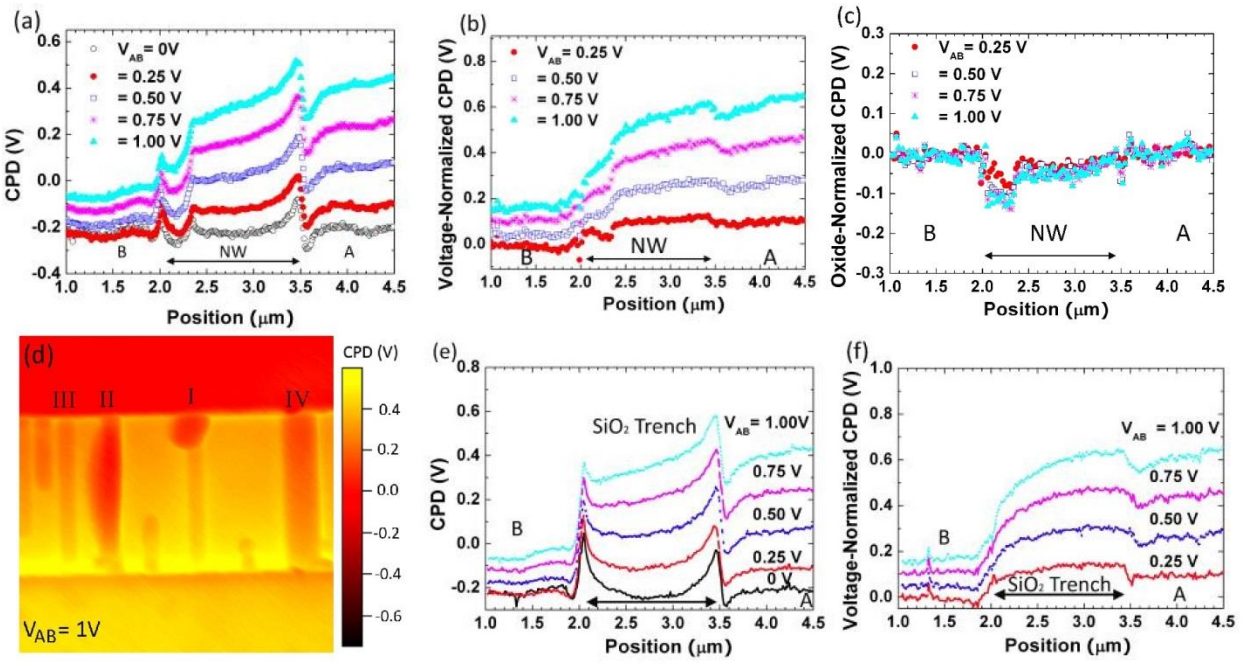

Figure 9 — Oxide Normalization : (a) Voltage line profiles across a broken NW (NW I shown in the KPFM image (d)), along with the corresponding voltage-normalized curve (b). The oxide-normalized curve is shown in (c). The oxide trench data used to compute the oxide-normalized curve is shown in (e), along with its corresponding voltage-normalized curve.

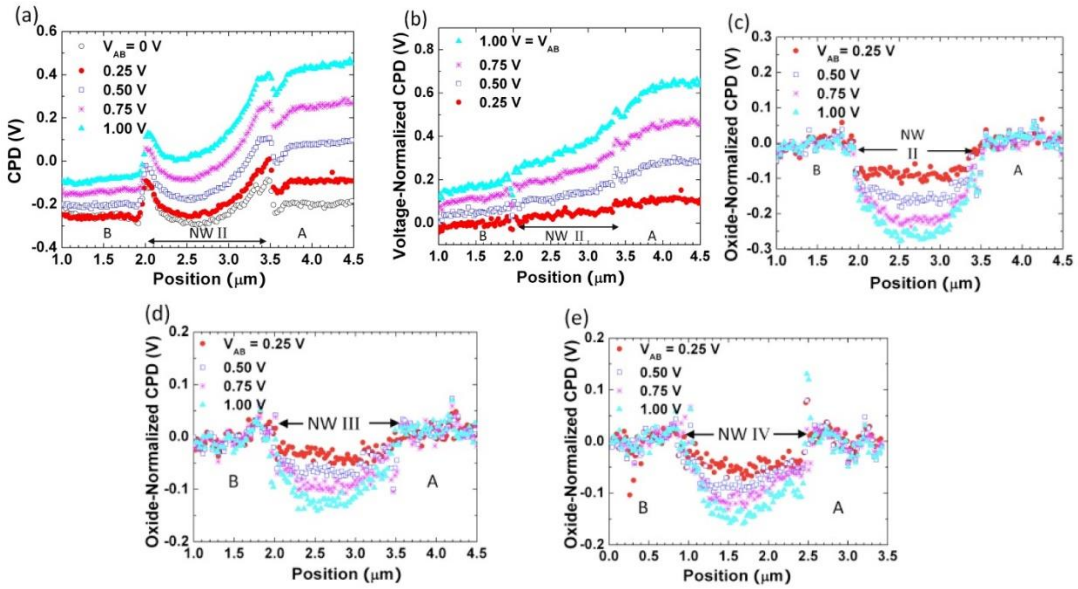

Figure 10 — Oxide Normalization of Current-Carrying NWs: (a) CPD line profiles across NW II shown in Figure 9(d), along with (b) voltage normalized and (c) oxide normalized curves for the same NW. Also pictured are oxide normalized line profiles for NWs (d) III and (e) IV respectively.

CHAPTER 4: BATCH ANALYSIS OF FS DATA

Computation of the Elastic Modulus of Tethered POPC LBMs

Lipid membranes are important in many topics in the biological sciences, including cell morphology[49], neurodegenerative disorders[50], viruses[51], and medicine[30,52,53]. Solid supports for lipid bilayer membranes (LBMs) provide a convenient two dimensional platform to facilitate the investigation of their physical properties[54–57].

Unilamellar vesicles composed of 1-palmitoyl-2-oleoyl-sn-glycero-3-phosphocholine (POPC) and functionalized with 1,2-distearoyl-sn-glycero-3-phosphoethanolamine-N-poly(ethylene glycol)-2000-N-[3-(2-pyridyldithio) propionate] (DSPE-PEG-PDP) with DSPE-PEG-PDP concentrations ranging between 0% and 24% were deposited on mica (vesicles with 0% DSPE-PEG-PDP) and gold (vesicles with >0% DSPE-PEG-PDP) substrates to investigate changes in the mechanical behavior of LBMs as the density of attached functional groups changes. FS was used to produce force-distance curves and least-squares fitting methods were used to numerically solve for the Young's modulus of the membranes.

Vesicles were produced using a series of freeze-thaw cycles followed by extrusion through porous membranes to make homogeneous vesicle suspensions. This process began with a solution in chloroform of POPC and DSPE-PEG-PDP with the desired molar ratios. These solutions were then dried at the bottom of a glass vial to remove chloroform, and then rehydrated with HEPES buffer solution to a lipid concentration of 5mM. This suspension was subjected to

freeze-thaw cycles and extruded through polycarbonate membranes with 100nm pores to produce suspended vesicles.

A tethered LBM (tLBM) is a membrane that is chemically bonded to a substrate. Non-tethered LBM systems were created by depositing pure POPC vesicles (0% DSPE-PEG-PDP) on freshly cleaved mica, and functionalized vesicles were deposited on template-stripped Au (TS-Au). The samples were all incubated at room temperature for 30 minutes to form large LBM domains.

These systems were probed using AFM and FS experiments performed on an Asylum Research MFP-3D-Bio AFM system, using Olympus OMCL-TR 400 PSA tips. Figure 11 shows AFM images of the tLBM systems. Figure 11(a) shows AFM topography maps of a bare TS-Au substrate with a root-mean-square roughness of less than 0.6nm. The POPC LBM shown in (b) displays high uniformity, and the DSPE-PEG-PDP functionalized tLBMs display large uniform domains in the concentration range from 2.5% to 10%. At 24% DSPE-PEG-PDP, however, domain boundaries can be seen, with domains ranging in size from 50nm to 400nm in diameter. These domains do not coincide with the domains of the TS-Au substrate shown in (a), indicating that this phenomenon is independent of the substrate surface morphology.

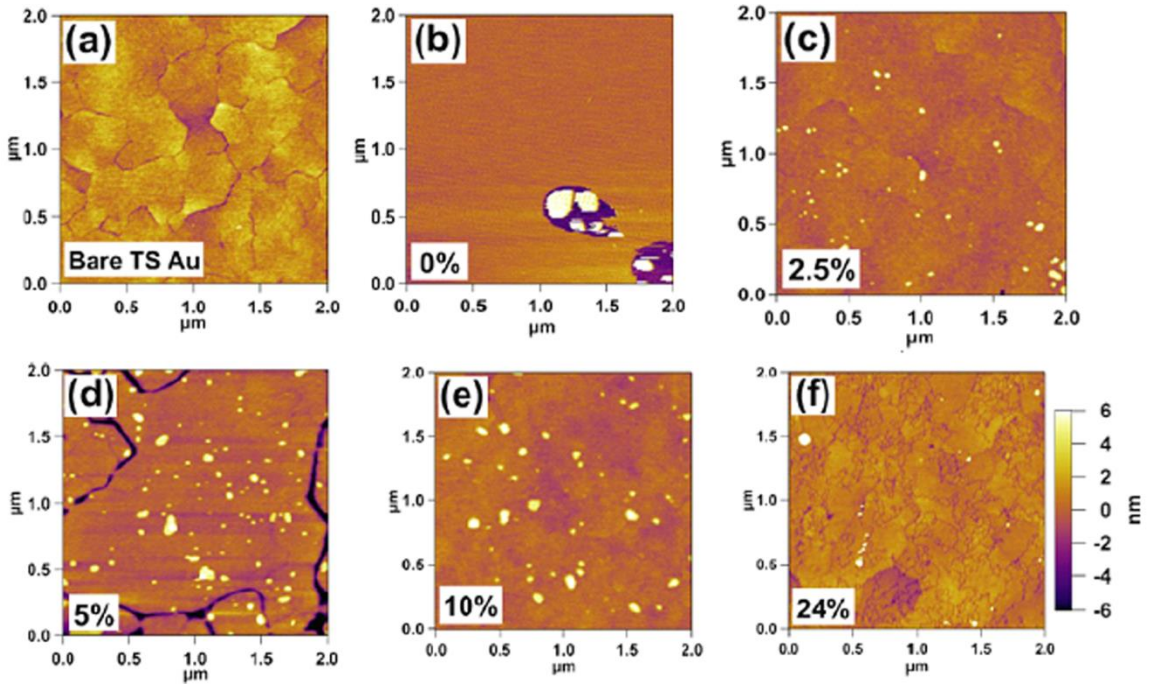

Figure 11 — AFM Topography of LBM Systems: (a) bare TS-Au used as the substrate for (c)-(f), (b) an un-functionalized LBM on mica and (c)-(f) LBMs with varying molar percentages of DSPE-PEG-PDP (2.5%, 5%, 10%, 24%) on TS-Au.

FS was performed on these systems, probing the mechanical behavior of tLBMs. To gain a statistically representative understanding of the sample system, a large number (n>150) of force-distance curves were analyzed for each concentration of DSPE-PEG-PDP using batch analysis. Using the algorithms outlined previously, the breakthrough distance, onset compression distance, and Young's modulus are calculated for each force-distance curve.

The calculated breakthrough and onset compression values are shown in Table 1. It is seen that the breakthrough distance for the non-functionalized LBMs is 2.9 nm. The breakthrough distance increases to approximately 4.5 nm when the concentration of DSPE-PEG-PDP is between 2.5% and 10%, and then decfreases to 3.5 nm at the higher concentration of 24%. The LBM thickness, or onset compression distance, has a value of 8.8nm for the POPC membrane, agreeing well with previous measurements of vesicle thickness[73], plus a 2 nm water

layer between LBM and substrate. For DSPE-PEG-PDP concentrations between 2.5% and 8% the LBM thickness increases to approximately 10 nm, decreasing to 9.4 nm at 10% concentration and further decreasing to 8.2 nm at 24% DSPE-PEG-PDP. The increase in thickness when the functional group is introduced can be attributed to an additional hydration layer due to the tethering molecules. The subsequent decrease in thickness signifies a structure change in the tethering molecule layer.

	0%	2.5%	5%	6%	8%	10%	24%
d_{BRK}	2.9 ± 0.4	5.0 ± 0.3	4.6 ± 0.5	4.1 ± 0.7	4.4 ± 0.8	4.8 ± 0.6	3.5 ± 0.5
d_{OC}	8.8 ± 1.1	11.0 ± 0.6	9.2 ± 0.9	9.6 ± 1.4	10.0 ± 1.2	9.4 ± 1.03	8.2 ± 1.0

Table 1 — Vesicle Size Data: Breakthrough distance and onset compression distance values (in nm) for the given molar concentration of DSPE-PEG-PDP.

This structure change can be observed in more detail by looking at the force-distance curves. Figure 12 shows sample curves for various concentrations of DSPE-PEG-PDP with a log-scale force axis. Taking the logarithm of the force enhances the initial tip-sample interaction region, allowing us to see the tip's longer range interactions with the LBM, including electrostatic interaction with the tethering molecules. The small magnitude of the exponential tail of the 0% data indicates the absence of tethering molecules, as expected. There is not a significant change in the 2.5% case, indicating that the tethering molecules are in the mushroom phase, reducing their long range interaction. In the 8% and 10% curves, there is an increase in magnitude of the long range interaction, reflecting the presence of brush phase tethering molecules, which are longer. As the concentration is raised to 24%, a reduction in long range force magnitude is seen, showing a reduction in the concentration of brush-phase tethering molecules. This change in tip-sample interaction in the 24% data along with the observed

formation of domain boundaries and changes in breakthrough distance and membrane thickness indicate a change in the structure of the POPC LBM system with increased concentrations of DSPE-PEG-PDP.

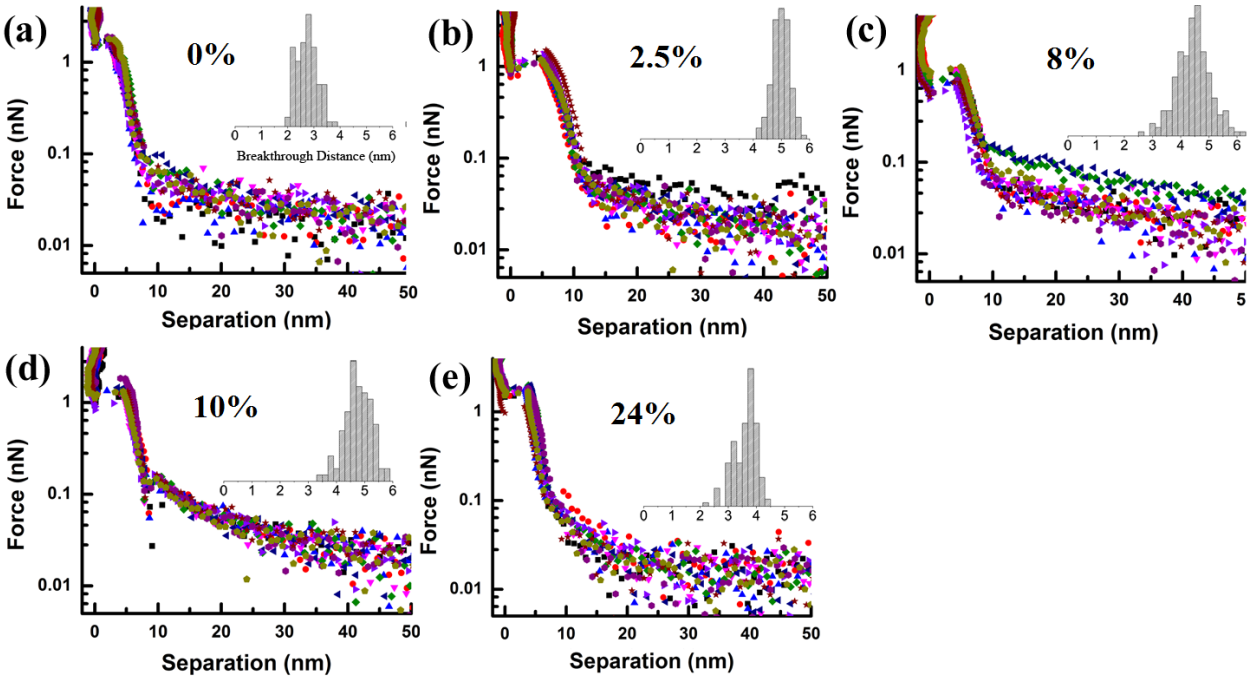

Figure 12 — Semilog Force-Distance Curves: Force-distance curves with a log-scale force axis for (a) 0%, (b) 2.5%, (c) 8%, (d) 10%, and (e) 24% DSPE-PEG-PDP. The insets are histograms of the breakthrough distance with the x-axis in nm.

The results of the Young's modulus calculations are shown in Figure 13. From the histograms, it is seen firstly that the calculated Young's modulus is nearly an order of magnitude smaller when using the BECC model as opposed to the Sneddon model. This is expected, since the BECC model corrects for the contribution of the rigid substrate to the apparent modulus. Furthermore, the histograms in (c) show narrower peaks, indicating that this model fits the data more accurately. The modulus trend shown in (d) shows an initial decrease in stiffness during the transition from 0% to 2.5%. This is due to the introduction of the tethering molecule cushioning layer between the LBM and TS-Au substrate. As the DSPE-PEG-PDP concentration is further

increased to 6%, E continues to decrease. This is due to disorder associated with the mushroom to brush transition of the tethering molecules. This explanation is also supported the abrupt increase in E at 8%, which is the result of the less compressible brush phase becoming the dominant phase of the tethering molecules.

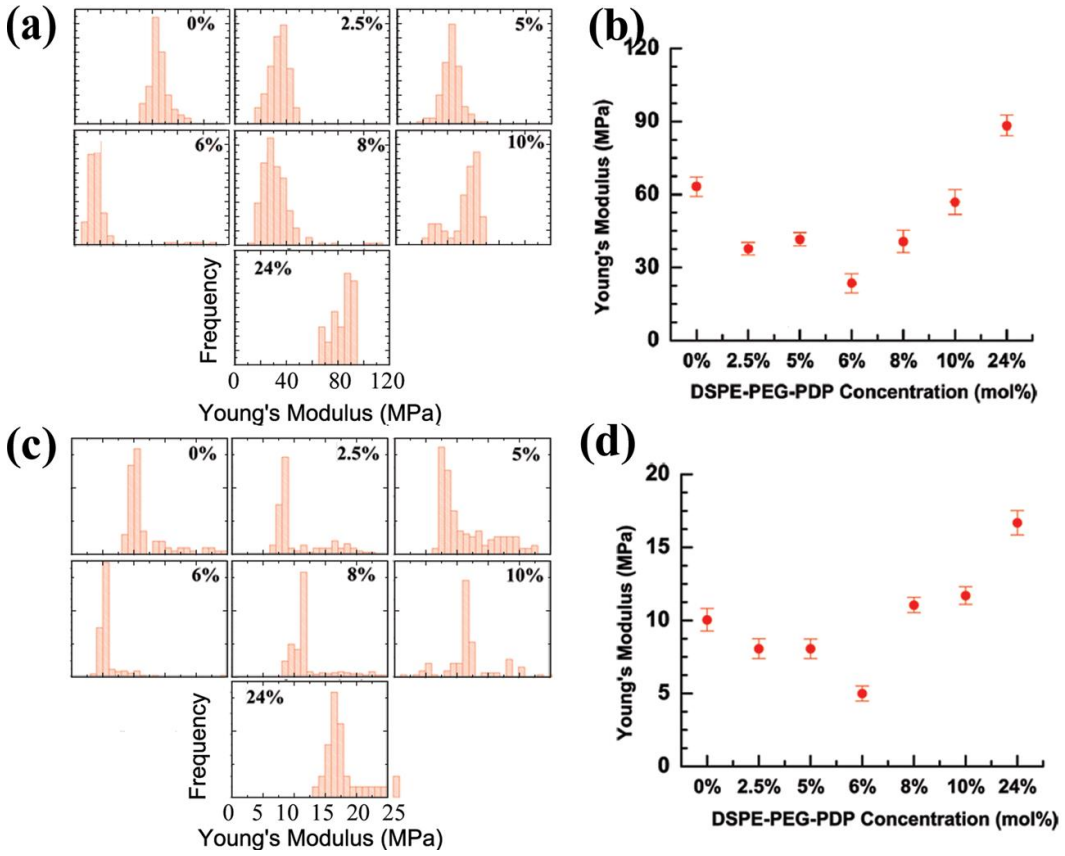

Figure 13 — Young's Modulus Results: Histograms of the Young's modulus calculated using (a) the Sneddon model and (c) the BECC model. The Young's modulus as a function of DSPE-PEG-PDP concentration is shown in (b) and (d) for the Sneddon and BECC models respectively.

The jump in E at 24% appears to show another phase transition, a hypothesis supported by the membrane thickness decrease seen in Table 1. This transition is believed to be the result of the PEG chains segregating to the edges of the flattened micelle domains observed in Figure 11(f) to stabilize the edges. This edge segregation has been previously reported for DSPE/PEG

and DSPC/PEG micelles[74,75]. The change in tLBM structure is shown schematically in Figure 14. With small concentrations of DSPE-PEG-PDP, the tethering molecules are spread out and are preferentially in the mushroom phase. Once the concentration of DSPE-PEG-PDP is raised to 8%, a phase transition occurs, and the tethering molecules reshape into the brush phase. At higher concentrations (~24%), there is another phase change, wherein the tLBM divides into flattened micelle domains, and DSPE-PEG-PDP groups congregate at the edges of these domains, leaving few tethering molecules on the flat regions of the tLBM.

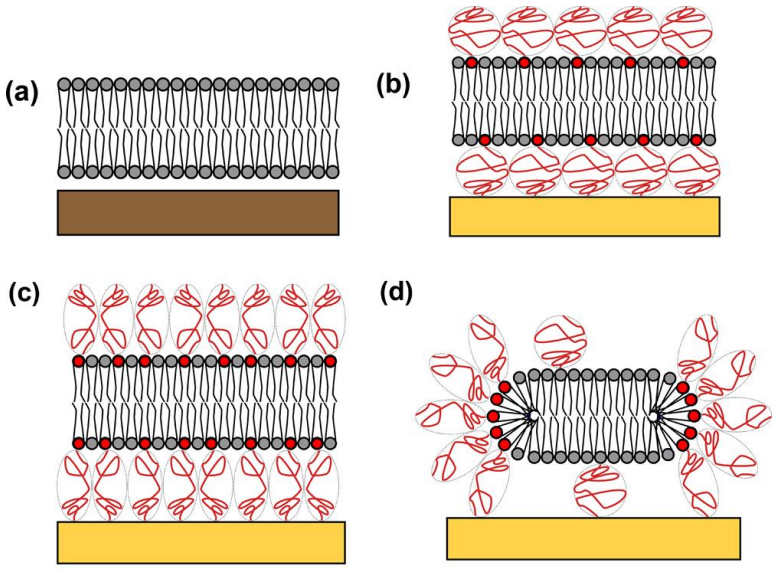

Figure 14 — Schematic of Tethered LBM Evolution: (a) Untethered LBM on mica. (b) Low concentration (1-6%) DSPE-PEG-PDP tLBM displaying mushroom phase conformation. (c) tLBMs with 8-10% DSPE-PEG-PDP, with tethering molecules in the brush phase. (d) High concentration (24%) DSPE-PEG-PDP, with tethering molecules preferentially segregating to micelle edges.

In this chapter, AFM force spectroscopy is used to determine the Young's moduli for tethered POPC LBMs with varying concentrations of tethering molecule DSPE-PEG-PDP, demonstrating the versatility of AFM FS as a stiffness measurement tool. It is found that the introduction of a PEG cushion layer decreases the measured stiffness of POPC membranes

relative to the membrane on a solid substrate without a cushion layer. There is a minimum in the measured stiffness at a DSPE-PEG-PDP concentration of 6%, corresponding to the disorder of the mushroom to brush transition. This minimum is followed by a sharp increase in stiffness due to the increased density of tethering molecules. Comparison of the two fitting models used on the data indicate that using the corrected BECC model decreases the measured stiffness and reduces the variance in the measured modulus due to the effect of the hard substrate being accounted for.

CHAPTER 5: CONCLUSIONS AND FUTURE WORK

Summary and Conclusions

The work in this thesis demonstrates the synergistic use of computational methods in conjunction with force microscopy experiments. FEM modeling was used to model the electrostatic interaction between KPFM probe tips and different surface potential distributions in VLS-grown Si NWs with applied bias to gain a quantitative understanding of experimental data. Additionally, algorithmic data analysis was applied to interpret large amounts of FS data taken from tLBM systems extracting the Young's modulus, membrane thickness, and breakthrough distance from experimental data. The work presented in this thesis shows the advantages of using computational methods in conjunction with force microscopy experiments.

AFM and KPFM experiments were performed on VLS NWs spanning an oxide trench between two electrodes using AFM. The electric potential across the NWs was varied to observe the local potential response using KPFM. KPFM CPD data along the NWs showed anomalous peaks near the ends of the nanowire trench. These peaks were found to be bias-independent, and voltage normalization was found to remove them entirely. To investigate the source of these peaks, this thesis presents results of FEM modeling. First, CPD line profiles were simulated for varying tip-sample separation, and it was found that surface tracking artifacts were not likely the source of these peaks. The simulations were repeated with charge inserted at the electrode/trench interface, and the simulated CPD data matched experiment well. Additionally, voltage normalization with the simulated data retrieved the expected NW potential response (a linear decrease in CPD across the NW). These FEM models lend support to the normalization methods

used to interpret experimental data, and are valuable tools during force microscopy experimentation.

FS data, consisting of hundreds of force-separation data sets, is convenient to analyze using computational methods. FS was performed on POPC membranes tethered to TS-AU substrates by synthesizing POPC unilamellar vesicles using varying concentrations of DSPE-PEG-PDP, and the breakthrough distance, membrane thickness, and Young's modulus of the membranes were tracked as a function of tethering molecule concentration. LBM systems are very variable, so statistically significant batches of data are necessary to gain an overall understanding of the properties of a membrane system. This makes the use of automated algorithmic data analysis helpful in extracting useful data from FS experiments. Algorithms were written to filter bad data curves and extract the breakthrough distance and membrane thickness, as well as to fit the low-indentation region of the data to two different models of the force versus indentation relation to determine the Young's modulus. By using these computational methods to analyze many sets of data, the mechanical properties of tLBM systems as a function of tethering molecule concentration were able to be determined with low statistical error.

The use of supplementary computations in conjunction with force probe experimentation has been demonstrated. FEM simulations help to elucidate the physical contributions to experimental data by starting from first principles. Batch analysis of data in FS allows for a reduction of statistical uncertainty by facilitating the processing of large amounts of data. Computational work should be considered whenever performing force microscopy experimentation to aid in understanding.

Future Work

This thesis has demonstrated the advantages of computational methods used to supplement force probe studies by discussing two systems, but there are many other opportunities to utilize this potent experimental tool.

Identification of Experimental Artifacts

In Chapter 3, a NW system was simulated using FEM simulations to prove that measured CPD spikes were not due to experimental artifacts. This procedure can be useful in most KPFM experiments. Due to the long-range nature of the electrostatic force relevant to KPFM, experimental artifacts are a nontrivial concern. FEM simulations of various sample geometries are a useful supplement to any KPFM experiment with nontrivial geometry. Once the theoretical CPD measurement for a given geometry is determined, the KPFM user can then focus on observing local variations in the CPD caused by work function changes and charges. This effectively increases the spatial resolution of KPFM.

KPFM of Nanodevices

The current-carrying NW system studied in this thesis were a good example of devices studied under operating conditions, but the presented methods can be applied to many different two-dimensional devices. KPFM of field-effect transistors, photovoltaics, and memristors, for instance, can yield important insights into their local electrical properties.

Tethered Lipid Bilayer Membranes as a Cell Model with Controllable Stiffness

The tLBM system highlighted in Chapter 4, due to its controllable stiffness, can be used to study the interactions of cell membranes with peptides and proteins. Biological systems are

complex, making the *in vivo* study of cell membrane interactions difficult. A model tLBM system allows for a streamlined study, isolating effects solely due to variations in the mechanical behavior of the membrane.

Bilayer Membrane Stability Studies

This thesis demonstrated a dependence of POPC membrane stiffness on the density of tethering molecules, however tLBM systems can be used as a platform for studying the impact on the stability of cell membranes caused by various biologically-relevant phenomena, such as the presence of pharmaceuticals, pH changes, or hormones. This system would allow for stiffness studies on a simplified tLBM system, as opposed to the more commonly used technique of probing the stiffness of whole living cells.

REFERENCES

(1) Binnig, G.; Quate, C. F.; Gerber, C. Atomic Force Microscope. *Phys. Rev. Lett.* **1986**, *56* (9), 930–933.

(2) Butt, H.-J.; Wolff, E. K.; Gould, S. A. C.; Dixon Northern, B.; Peterson, C. M.; Hansma, P. K. Imaging Cells with the Atomic Force Microscope. *J. Struct. Biol.* **1990**, *105* (1–3), 54–61.

(3) Calò, A.; Reguera, D.; Oncins, G.; Persuy, M.-A.; Sanz, G.; Lobasso, S.; Corcelli, A.; Pajot-Augy, E.; Gomila, G. Force Measurements on Natural Membrane Nanovesicles Reveal a Composition-Independent, High Young's Modulus. *Nanoscale* **2014**, *6* (4), 2275.

(4) Lekka, M.; Laidler, P.; Gil, D.; Lekki, J.; Stachura, Z.; Hrynkiewicz, A. Z. Elasticity of Normal and Cancerous Human Bladder Cells Studied by Scanning Force Microscopy. *Eur. Biophys. J.* **1999**, *28* (4), 312–316.

(5) Lekka, M.; Pogoda, K.; Gostek, J.; Klymenko, O.; Prauzner-Bechcicki, S.; Wiltowska-Zuber, J.; Jaczewska, J.; Lekki, J.; Stachura, Z. Cancer Cell Recognition – Mechanical Phenotype. *Micron* **2012**, *43* (12), 1259–1266.

(6) Prabhune, M.; Belge, G.; Dotzauer, A.; Bullerdiek, J.; Radmacher, M. Comparison of Mechanical Properties of Normal and Malignant Thyroid Cells. *Micron* **2012**, *43* (12), 1267–1272.

(7) Alessandrini, A.; Facci, P. Nanoscale Mechanical Properties of Lipid Bilayers and Their Relevance in Biomembrane Organization and Function. *Micron* **2012**, *43* (12), 1212–1223.

(8) Li, S.; Eghiaian, F.; Sieben, C.; Herrmann, A.; Schaap, I. A. T. Bending and Puncturing the Influenza Lipid Envelope. *Biophys. J.* **2011**, *100* (3), 637–645.

(9) Ouyang, W.; Shinde, A.; Zhang, Y.; Cao, J.; Ragan, R.; Wu, R. Structural and Chemical Properties of Gold Rare Earth Disilicide Core−Shell Nanowires. *ACS Nano* **2011**, *5* (1), 477–485.

(10) Sasahara, A.; Pang, C. L.; Onishi, H. Local Work Function of Pt Clusters Vacuum-Deposited on a TiO2 Surface. *J. Phys. Chem. B* **2006**, *110* (35), 17584–17588.

(11) Hiehata, K.; Sasahara, A.; Onishi, H. Local Work Function Analysis of Pt/TiO2 Photocatalyst by a Kelvin Probe Force Microscope. *Nanotechnology* **2007**, *18*, 084007.

(12) Koren, E.; Rosenwaks, Y.; Allen, J. E.; Hemesath, E. R.; Lauhon, L. J. Nonuniform Doping Distribution along Silicon Nanowires Measured by Kelvin Probe Force Microscopy and Scanning Photocurrent Microscopy. *Appl. Phys. Lett.* **2009**, *95* (9), 092105.

(13) Koren, E.; Elias, G.; Boag, A.; Hemesath, E. R.; Lauhon, L. J.; Rosenwaks, Y. Direct Measurement of Individual Deep Traps in Single Silicon Nanowires. *Nano Lett.* **2011**, *11* (6), 2499–2502.

(14) Henning, A. K.; Hochwitz, T.; Slinkman, J.; Never, J.; Hoffmann, S.; Kaszuba, P.; Daghlian, C. Two-dimensional Surface Dopant Profiling in Silicon Using Scanning Kelvin Probe Microscopy. *J. Appl. Phys.* **1995**, *77* (5), 1888–1896.

(15) Robin, F.; Jacobs, H.; Homan, O.; Stemmer, A.; Bächtold, W. Investigation of the Cleaved Surface of a P–i–n Laser Using Kelvin Probe Force Microscopy and Two-Dimensional Physical Simulations. *Appl. Phys. Lett.* **2000**, *76* (20), 2907–2909.

(16) Mizutani, T.; Arakawa, M.; Kishimoto, S. Two-Dimensional Potential Profile Measurement of GaAs HEMT's by Kelvin Probe Force Microscopy. *IEEE Electron Device Lett.* **1997**, *18* (9), 423–425.

(17) Bae, S. S.; Prokopuk, N.; Quitoriano, N. J.; Adams, S. M.; Ragan, R. Characterizing Defects and Transport in Si Nanowire Devices Using Kelvin Probe Force Microscopy. *Nanotechnology* **2012**, *23* (40), 405706.

(18) Batko, I.; Batkova, M. Memristive Behavior of Nb/NbOx/Nb Structures Prepared by Local Anodic Oxidation1. *Mater. Today Proc.* **2016**, *3* (3), 803–809.

(19) Neff, J. L.; Rahe, P. Insights into Kelvin Probe Force Microscopy Data of Insulator-Supported Molecules. *Phys. Rev. B* **2015**, *91* (8), 085424.

(20) Yun, J. S.; Ho-Baillie, A.; Huang, S.; Woo, S. H.; Heo, Y.; Seidel, J.; Huang, F.; Cheng, Y.-B.; Green, M. A. Benefit of Grain Boundaries in Organic–Inorganic Halide Planar Perovskite Solar Cells. *J. Phys. Chem. Lett.* **2015**, *6* (5), 875–880.

(21) Fuchs, F.; Caffy, F.; Demadrille, R.; Mélin, T.; Grévin, B. High-Resolution Kelvin Probe Force Microscopy Imaging of Interface Dipoles and Photogenerated Charges in Organic Donor–Acceptor Photovoltaic Blends. *ACS Nano* **2016**, *10* (1), 739–746.

(22) Szwajca, A.; Wei, J.; Schukfeh, M. I.; Tornow, M. Self-Assembled Monolayers of Alkyl-Thiols on InAs: A Kelvin Probe Force Microscopy Study. *Surf. Sci.* **2015**, *633*, 53–59.

(23) Jöhr, R.; Hinaut, A.; Pawlak, R.; Sadeghi, A.; Saha, S.; Goedecker, S.; Such, B.; Szymonski, M.; Meyer, E.; Glatzel, T. Characterization of Individual Molecular Adsorption Geometries by Atomic Force Microscopy: Cu-TCPP on Rutile TiO2 (110). *J. Chem. Phys.* **2015**, *143* (9), 094202.

(24) Ryu, S. R.; Ram, S. D. G.; Lee, S. J.; Cho, H.; Lee, S.; Kang, T. W.; Kwon, S.; Yang, W.; Shin, S.; Woo, Y. Vertical Current-Flow Enhancement via Fabrication of GaN Nanorod P–n Junction Diode on Graphene. *Appl. Surf. Sci.* **2015**, *347*, 793–798.

(25) Halpern, E.; Henning, A.; Shtrikman, H.; Rurali, R.; Cartoixà, X.; Rosenwaks, Y. Room Temperature Observation of Quantum Confinement in Single InAs Nanowires. *Nano Lett.* **2015**, *15* (1), 481–485.

(26) Zhang, Y.; Pluchery, O.; Caillard, L.; Lamic-Humblot, A.-F.; Casale, S.; Chabal, Y. J.; Salmeron, M. Sensing the Charge State of Single Gold Nanoparticles via Work Function Measurements. *Nano Lett.* **2015**, *15* (1), 51–55.

(27) Kuznetsova, T. G.; Starodubtseva, M. N.; Yegorenkov, N. I.; Chizhik, S. A.; Zhdanov, R. I. Atomic Force Microscopy Probing of Cell Elasticity. *Micron* **2007**, *38* (8), 824–833.

(28) Ikai, A. A Review on: Atomic Force Microscopy Applied to Nano-Mechanics of the Cell. In *Nano/Micro Biotechnology*; Endo, I., Nagamune, T., Eds.; Advances in Biochemical Engineering / Biotechnology; Springer Berlin Heidelberg, 2009; pp 47–61.

(29) Yang, L.; Tan, X.; Wang, Z.; Zhang, X. Supramolecular Polymers: Historical Development, Preparation, Characterization, and Functions. *Chem. Rev.* **2015**, *115* (15), 7196–7239.

(30) Bozzuto, G.; Molinari, A. Liposomes as Nanomedical Devices. *Int. J. Nanomedicine* **2015**, 975.

(31) Lacey, S. D.; Wan, J.; Cresce, A. von W.; Russell, S. M.; Dai, J.; Bao, W.; Xu, K.; Hu, L. Atomic Force Microscopy Studies on Molybdenum Disulfide Flakes as Sodium-Ion Anodes. *Nano Lett.* **2015**, *15* (2), 1018–1024.

(32) Cymer, F.; von Heijne, G.; White, S. H. Mechanisms of Integral Membrane Protein Insertion and Folding. *J. Mol. Biol.* **2015**, *427* (5), 999–1022.

(33) Jacobs, H. O.; Leuchtmann, P.; Homan, O. J.; Stemmer, A. Resolution and Contrast in Kelvin Probe Force Microscopy. *J. Appl. Phys.* **1998**, *84* (3), 1168–1173.

(34) Baier, R.; Leendertz, C.; Lux-Steiner, M. C.; Sadewasser, S. Toward Quantitative Kelvin Probe Force Microscopy of Nanoscale Potential Distributions. *Phys. Rev. B* **2012**, *85* (16).

(35) Hudlet, S.; Saintjean, M.; Roulet, B.; Berger, J.; Guthmann, C. Electrostatic Forces Between Metallic Tip and Semiconductor Surfaces. *J. Appl. Phys.* **1995**, *77* (7), 3308–3314.

(36) Dimitriadis, E. K.; Horkay, F.; Maresca, J.; Kachar, B.; Chadwick, R. S. Determination of Elastic Moduli of Thin Layers of Soft Material Using the Atomic Force Microscope. *Biophys. J.* **2002**, *82* (5), 2798–2810.

(37) Stetter, F. W. S.; Hugel, T. The Nanomechanical Properties of Lipid Membranes Are Significantly Influenced by the Presence of Ethanol. *Biophys. J.* **2013**, *104* (5), 1049–1055.

(38) Sadewasser, S.; Leendertz, C.; Streicher, F.; Lux-Steiner, M. C. The Influence of Surface Topography on Kelvin Probe Force Microscopy. *Nanotechnology* **2009**, *20* (50), 505503.

(39) Tsukada, M.; Masago, A.; Shimizu, M. Theoretical Simulation of Kelvin Probe Force Microscopy for Si Surfaces by Taking Account of Chemical Forces. *J. Phys. Condens. Matter Inst. Phys. J.* **2012**, *24* (8), 084002.

(40) Wang, Z. L.; Song, J. Piezoelectric Nanogenerators Based on Zinc Oxide Nanowire Arrays. *Science* **2006**, *312* (5771), 242–246.

(41) Huang, M. H.; Mao, S.; Feick, H.; Yan, H.; Wu, Y.; Kind, H.; Weber, E.; Russo, R.; Yang, P. Room-Temperature Ultraviolet Nanowire Nanolasers. *Science* **2001**, *292* (5523), 1897–1899.

(42) Zhu, H.; Fu, Y.; Meng, F.; Wu, X.; Gong, Z.; Ding, Q.; Gustafsson, M. V.; Trinh, M. T.; Jin, S.; Zhu, X.-Y. Lead Halide Perovskite Nanowire Lasers with Low Lasing Thresholds and High Quality Factors. *Nat. Mater.* **2015**, *14* (6), 636–642.

(43) Yu, Z.; Tetard, L.; Zhai, L.; Thomas, J. Supercapacitor Electrode Materials: Nanostructures from 0 to 3 Dimensions. *Energy Environ. Sci.* **2015**, *8* (3), 702–730.

(44) Tang, C.; Cheng, N.; Pu, Z.; Xing, W.; Sun, X. NiSe Nanowire Film Supported on Nickel Foam: An Efficient and Stable 3D Bifunctional Electrode for Full Water Splitting. *Angew. Chem. Int. Ed.* **2015**, *54* (32), 9351–9355.

(45) Yin, H.; Zhao, S.; Zhao, K.; Muqsit, A.; Tang, H.; Chang, L.; Zhao, H.; Gao, Y.; Tang, Z. Ultrathin Platinum Nanowires Grown on Single-Layered Nickel Hydroxide with High Hydrogen Evolution Activity. *Nat. Commun.* **2015**, *6*, 6430.

(46) Liu, Z.; Xu, J.; Chen, D.; Shen, G. Flexible Electronics Based on Inorganic Nanowires. *Chem. Soc. Rev.* **2014**, *44* (1), 161–192.

(47) Yu, R.; Wu, W.; Pan, C.; Wang, Z.; Ding, Y.; Wang, Z. L. Piezo-Phototronic Boolean Logic and Computation Using Photon and Strain Dual-Gated Nanowire Transistors. *Adv. Mater.* **2015**, *27* (5), 940–947.

(48) Morkötter, S.; Jeon, N.; Rudolph, D.; Loitsch, B.; Spirkoska, D.; Hoffmann, E.; Döblinger, M.; Matich, S.; Finley, J. J.; Lauhon, L. J.; Abstreiter, G.; Koblmüller, G. Demonstration of Confined Electron Gas and Steep-Slope Behavior in Delta-Doped GaAs-AlGaAs Core–Shell Nanowire Transistors. *Nano Lett.* **2015**, *15* (5), 3295–3302.

(49) McMahon, H. T.; Boucrot, E. Membrane Curvature at a Glance. *J Cell Sci* **2015**, *128* (6), 1065–1070.

(50) Galvagnion, C.; Buell, A. K.; Meisl, G.; Michaels, T. C. T.; Vendruscolo, M.; Knowles, T. P. J.; Dobson, C. M. Lipid Vesicles Trigger α-Synuclein Aggregation by Stimulating Primary Nucleation. *Nat. Chem. Biol.* **2015**, *11* (3), 229–234.

(51) Perlmutter, J. D.; Hagan, M. F. Mechanisms of Virus Assembly. *Annu. Rev. Phys. Chem.* **2015**, *66* (1), 217–239.

(52) Sakurai, Y.; Kolokoltsov, A. A.; Chen, C.-C.; Tidwell, M. W.; Bauta, W. E.; Klugbauer, N.; Grimm, C.; Wahl-Schott, C.; Biel, M.; Davey, R. A. Two-Pore Channels Control Ebola Virus Host Cell Entry and Are Drug Targets for Disease Treatment. *Science* **2015**, *347* (6225), 995–998.

(53) Kathawala, R. J.; Gupta, P.; Ashby, C. R.; Chen, Z.-S. The Modulation of ABC Transporter-Mediated Multidrug Resistance in Cancer: A Review of the Past Decade. *Drug Resist. Updat.* **2015**, *18*, 1–17.

(54) Cornell, B. A.; Braach-Maksvytis, V. L.; King, L. G.; Osman, P. D.; Raguse, B.; Wieczorek, L.; Pace, R. J. A Biosensor That Uses Ion-Channel Switches. *Nature* **1997**, *387* (6633), 580–583.

(55) Naumann, C. A.; Prucker, O.; Lehmann, T.; Rühe, J.; Knoll, W.; Frank, C. W. The Polymer-Supported Phospholipid Bilayer: Tethering as a New Approach to Substrate-Membrane Stabilization. *Biomacromolecules* **2002**, *3* (1), 27–35.

(56) Kühner, M.; Tampé, R.; Sackmann, E. Lipid Mono- and Bilayer Supported on Polymer Films: Composite Polymer-Lipid Films on Solid Substrates. *Biophys. J.* **1994**, *67* (1), 217–226.

(57) Wagner, M. L.; Tamm, L. K. Tethered Polymer-Supported Planar Lipid Bilayers for Reconstitution of Integral Membrane Proteins: Silane-Polyethyleneglycol-Lipid as a Cushion and Covalent Linker. *Biophys. J.* **2000**, *79* (3), 1400–1414.

(58) Albrecht, T. R.; Grütter, P.; Horne, D.; Rugar, D. Frequency Modulation Detection Using high-Q Cantilevers for Enhanced Force Microscope Sensitivity. *J. Appl. Phys.* **1991**, *69* (2), 668–673.

(59) Cohen, G.; Halpern, E.; Nanayakkara, S. U.; Luther, J. M.; Held, C.; Bennewitz, R.; Boag, A.; Rosenwaks, Y. Reconstruction of Surface Potential from Kelvin Probe Force Microscopy Images. *Nanotechnology* **2013**, *24* (29), 295702.

(60) Colchero, J.; Gil, A.; Baró, A. M. Resolution Enhancement and Improved Data Interpretation in Electrostatic Force Microscopy. *Phys. Rev. B* **2001**, *64* (24), 245403.

(61) Leendertz, C.; Streicher, F.; Lux-Steiner, M. C.; Sadewasser, S. Evaluation of Kelvin Probe Force Microscopy for Imaging Grain Boundaries in Chalcopyrite Thin Films. *Appl. Phys. Lett.* **2006**, *89* (11), 113120-113120–113123.

(62) Masago, A.; Tsukada, M.; Shimizu, M. Simulation Method of Kelvin Probe Force Microscopy at Nanometer Range and Its Application. *Phys. Rev. B* **2010**, *82* (19), 195433.

(63) Belaidi, S.; Lebon, F.; Girard, P.; Leveque, G.; Pagano, S. Finite Element Simulations of the Resolution in Electrostatic Force Microscopy. *Appl. Phys. A* **1998**, *66* (1), S239–S243.

(64) Baier, R.; Leendertz, C.; Lux-Steiner, M. C.; Sadewasser, S. Toward Quantitative Kelvin Probe Force Microscopy of Nanoscale Potential Distributions. *Phys. Rev. B* **2012**, *85* (16).

(65) Schmidt, S. S.; Abou-Ras, D.; Sadewasser, S.; Yin, W.; Feng, C.; Yan, Y. Electrostatic Potentials at Cu(In,Ga)Se_{2} Grain Boundaries: Experiment and Simulations. *Phys. Rev. Lett.* **2012**, *109* (9), 095506.

(66) Heinz, W. F.; Hoh, J. H. Spatially Resolved Force Spectroscopy of Biological Surfaces Using the Atomic Force Microscope. *Trends Biotechnol.* **1999**, *17* (4), 143–150.

(67) Sneddon, I. N. The Relation between Load and Penetration in the Axisymmetric Boussinesq Problem for a Punch of Arbitrary Profile. *Int. J. Eng. Sci.* **1965**, *3* (1), 47–57.

(68) Marcu, A.; Nicolae, I.; Viespe, C. Active Surface Geometrical Control of Noise in Nanowire-SAW Sensors. *Sens. Actuators B Chem.* **2016**, *231*, 469–473.

(69) Thomas, R.; Rao, G. M. SnO2 Nanowire Anchored Graphene Nanosheet Matrix for the Superior Performance of Li-Ion Thin Film Battery Anode. *J. Mater. Chem. A* **2014**, *3* (1), 274–280.

(70) Misra, S.; Yu, L.; Foldyna, M.; Cabarrocas, P. R. i. New Approaches to Improve the Performance of Thin-Film Radial Junction Solar Cells Built Over Silicon Nanowire Arrays. *IEEE J. Photovolt.* **2015**, *5* (1), 40–45.

(71) Quitoriano, N. J.; Kamins, T. I. Integratable Nanowire Transistors. *Nano Lett.* **2008**, *8* (12), 4410–4414.

(72) Barrett, R. C.; Quate, C. F. Charge Storage in a Nitride-oxide-silicon Medium by Scanning Capacitance Microscopy. *J. Appl. Phys.* **1991**, *70* (5), 2725–2733.

(73) Heberle, F. A.; Petruzielo, R. S.; Pan, J.; Drazba, P.; Kučerka, N.; Standaert, R. F.; Feigenson, G. W.; Katsaras, J. Bilayer Thickness Mismatch Controls Domain Size in Model Membranes. *J. Am. Chem. Soc.* **2013**, *135* (18), 6853–6859.

(74) Johnsson, M.; Edwards, K. Liposomes, Disks, and Spherical Micelles: Aggregate Structure in Mixtures of Gel Phase Phosphatidylcholines and Poly(ethylene Glycol)-Phospholipids. *Biophys. J.* **2003**, *85* (6), 3839–3847.

(75) Mazer, N. A.; Benedek, G. B.; Carey, M. C. Quasielastic Light-Scattering Studies of Aqueous Biliary Lipid Systems. Mixed Micelle Formation in Bile Salt-Lecithin Solutions. *Biochemistry (Mosc.)* **1980**, *19* (4), 601–615.